Bio-Design and Manufacturing (2021) 4:879–888
https://doi.org/10.1007/s42242-021-00147-2

RESEARCH ARTICLE

In vivo analysis of post-joint-preserving surgery fracture of 3D-printed Ti-6Al-4V implant to treat bone cancer

Jong Woong Park[1,2] · Ye Chan Shin[1] · Hyun Guy Kang[1,2] · Sangeun Park[3] · Eunhyeok Seo[4] · Hyokyung Sung[3] · Im Doo Jung[4]

Received: 1 March 2021 / Accepted: 9 June 2021 / Published online: 6 July 2021

Abstract

Cancer growth in the bone due to its random shape disables bone strength and thus changes its capacity to support body weight or muscles, which can crucially affect the quality of human life in terms of normal walking or daily activities. For successful patient recovery, it is necessary to remove the cancer-affected minimal bone area and quickly replace it with a biocompatible metal implant within less than 2 weeks. An electron beam-melted Ti-6Al-4V implant was designed and applied in a patient to preserve the natural knee joint close to the bone tumor. The developed implant fits the bone defect well, and the independent ambulatory function of the natural knee joint was restored in the patient within six weeks after surgery. A delayed fracture occurred six months after the successful replacement of cancer-affected bone with Ti-6Al-4V implant at the proximal meshed junction of the implant because of a minor downward slip. Microstructural, mechanical, and computational analyses were conducted for the fractured area to find the main reason for the delayed fracture. Our findings pertaining to the mechanical and material investigation can help realize the safe implantation of the three-dimensionally printed titanium implant to preserve the natural joints of patients with massive bone defects of the extremities.

Keywords 3D printing · Bone cancer · Titanium alloy implant · Electron beam melting · Fracture analysis

Introduction

3D printing is an important manufacturing technology to fabricate objects with a net shape in a single process through the adhesion of various materials [1–3]. Owing to the benefit of the customizable net shape fabrication method, the 3D printing process has been widely applied in practical medical research from customized artificial organs to teeth or bones [4–16]. In the field of practical orthopedic surgery, metal 3D printing is more often utilized. In particular, metal implants to replace bone tissue can be manufactured relatively easily, as these are solid. Orthopedic 3D-printed implants are often constructed using the electron beam melting (EBM) process, which imparts desirable mechanical properties to the fabricated implants by printing at relatively high temperatures [17, 18]. Malignant bone tumors of the extremities constitute a life-threatening condition, and functional limb disability may occur even if the patient survives. The key treatment for localized malignant bone tumors is to surgically remove the cancer with a wide margin, which involves normal tissue surrounding the tumor. This tumor removal surgery approach, known as wide excision, often results in severe bone and soft tissue defects.

Reconstruction surgery is performed to minimize the functional deficit after wide excision, with the entire process known as limb salvage surgical process in the orthopedic oncology domain. The bone tissue is commonly replaced using conventional modular-type metal implants (endoprostheses) [19–21]. During implementing an endoprosthesis,

✉ Hyokyung Sung
hksung@gnu.ac.kr

✉ Im Doo Jung
idjung@unist.ac.kr

1 Division of Convergence Technology, National Cancer Center, Goyang 10408, Republic of Korea

2 Orthopaedic Oncology Clinic, National Cancer Center, Goyang 10408, Republic of Korea

3 Department of Materials Engineering and Convergence Technology, Gyeongsang National University, Jin-Ju 52828, Republic of Korea

4 Department of Mechanical Engineering, Ulsan National Institute of Science and Technology, UNIST-Gil 50, Ulsan 44919, Republic of Korea

when the amount of the remaining normal bone is excessively small after the wide excision of the bone tumor, the adjacent joint that is not affected by the tumor may be sacrificed to fix the implant. Nevertheless, preserving natural joints is highly beneficial for proper joint function and longevity [22, 23]. In this regard, joint preservation can be realized by using a personalized implant for the patient, thereby minimizing functional loss.

Although the concept of a patient-customized implant is not new, it has been promoted with the advancement of additive manufacturing (AM). In general, personalized implants fabricated through metal casting cannot be widely applied owing to the associated high cost and considerable production time. A customized implant to be used for cancer patients should not take too long to fabricate to avoid the tumor from progressing excessively before surgical treatment is realized. A personalized titanium alloy implant can be fabricated through 3D printing in approximately three weeks [24]. Many researchers have reported promising surgical results for limb salvage operations using 3D-printed customized metal implants made of Ti-6Al-4V [25–27]. However, certain concerns remain with respect to the lack of long-term clinical outcomes and experience. Since sufficient time must elapse to evaluate long-term surgical results, it is critical to thoroughly investigate cases of mechanical failure to enhance the implant design and quality.

In this study, a titanium implant was designed and printed using the EBM technique, and surgery was performed to remove a tumor in the long bone of a patient while preserving the natural joint at the knee. Following the fracture of the implant six months after surgery, fracture analysis along with a mechanical and microstructural in-depth investigation of the damaged implant was performed.

Materials and methods

The implant was manufactured using an EBM type 3D printer (ARCAM A1, Arcam AB, Sweden). The material used was Ti-6Al-4V alloy powder (Arcam AB, size 45–106 μm), and the mesh body (lattice) had a Dode-Thin structure. The process conditions were as follows: electron beam power of 50–3000 W, scan speed of 4530 m/s, and layer thickness of 50 μm. To evaluate the mechanical properties under these process conditions, the tensile specimens were fabricated according to the ASTM-E8/E8M standard (round-type and plate-type). Tensile tests were performed using a universal test machine (Minos-100, MTDI) with a load cell capacity of 100 kN under quasi-static conditions, and a displacement control velocity of 3 mm/min. The round-type specimens featured a length, diameter, and gauge length of 140, 12.5, and 50 mm, respectively, and the plate-type specimens had a length, width, and thickness of 200, 25, and 6 mm, respectively.

In order to investigate the mechanical behavior of the mesh structure, the Dode-Thin type structure was applied along the gauge length of the plate-type specimens. The corresponding microstructures were analyzed by the electron backscatter diffraction (EBSD) technique, and the

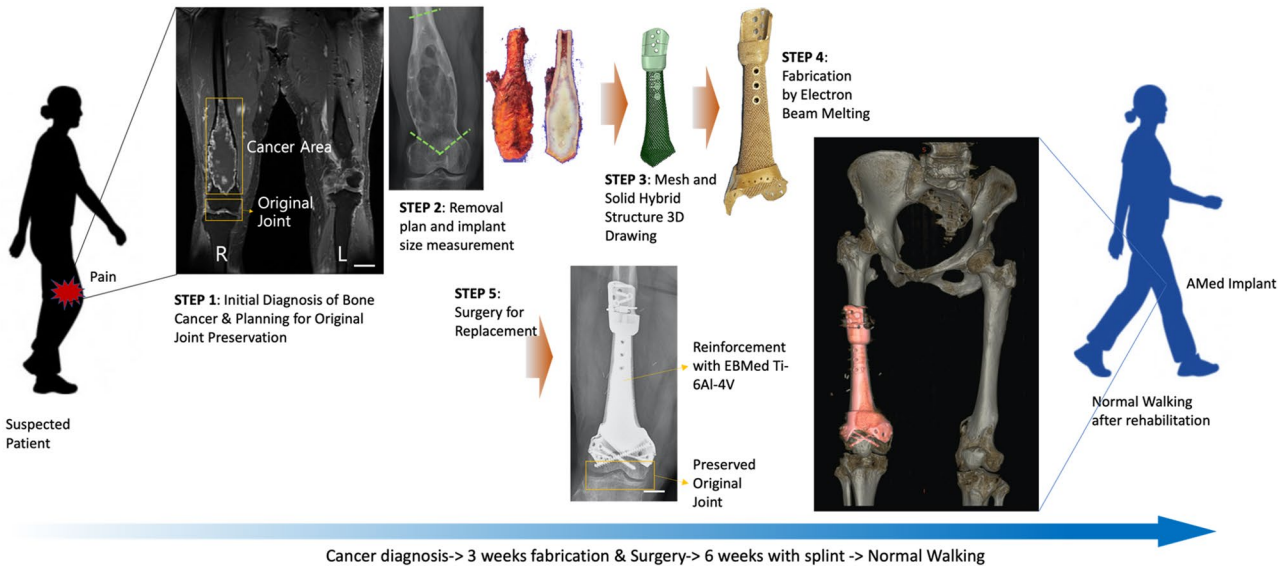

Fig. 1 Surgical procedure of surgery for bone tumor with additively manufactured Ti-6Al-4V implant. Step 1: Initial diagnosis of bone cancer and surgery planning for original joint preservation. Step 2: Cancer removal plan and implant size measurement. Step 3: Design of artificial implant with mesh and solid hybrid structure. Step 4: Electron beam melting process with Ti-6Al-4V. Step 5: Embedding surgery of electron beam-melted Ti-6Al-4V implant into the area of removed cancer bone, and suturing

aggregation formation and tensile deformation behavior were subsequently studied. The EBSD analysis was conducted using a field emission scanning electron microscope (MIRA I LMH) with a power of 20 kV and step size of 0.5 µm. In addition, the effects of the micropores, unmelt powder, and lack of fusion pores on the tensile behavior were examined by performing a tensile fracture surface analysis.

Results and discussion

The cancerous tumor, chondrosarcoma was formed in the local area of the long bone of the patient's left leg, while the near knee joint bone was safe from malignancy. For the survival of the natural knee joint, rather than using a commercial standardized implant, customized 3D-printed titanium implant was planned to replace the local cancer-affected area. For the surgery to be successful, the implant had to meet three major requirements: (1) A hybrid structure with a suitable proportion of mesh for muscle bonding and a solid area for the protection of nerves from scratches; (2) Strength to withstand repeated long-term physiological loading; (3) Conformity with other body elements to act as an actual living bone tissue. The schematic diagram of implant development and the actual surgery considering the major requirements of the artificial implant is illustrated in Fig. 1. STEP 1: The bone cancer in the local area of long bone is accurately diagnosed. STEP 2: The morphology of cancer-affected bone area is designated for removal while maintaining the natural knee joint. STEP 3: 3D graphical prototyping is performed to match the empty bone area with mesh and solid hybrid structured implant. STEP 4: EBM and post-processing for biocompatibility are performed to fabricate the Ti-6Al-4V implant. Finally, long bone surgery is performed using the printed/post-processed Ti-6Al-4V implant with proximal and distal fixation at the bone defect through the tumor excision.

Using the 3D printed Ti-6Al-4V implant, the patient was able to walk with her natural knee joint and resume living a normal life after six weeks from surgery. Moreover, the leg length discrepancy was partially corrected and thus walking was more comfortable for the patient than pre-surgery because their heels were touching the ground while standing and walking [28, 29]. However, as shown in Fig. 2, due to a mild downward slip half a year later, the Ti-6Al-4V implant suffered fracture at the junction between the implant body and the proximal fixation plate, specifically, the connection between the head and the body part. The fracture between the implant head and body can be clearly seen in the 3D computed tomography reconstruction image and the X-ray image, depicted in Fig. 2a and 2b. The fractured top part is shown in Fig. 2c with a note on the solid-mesh connection boundary and the center. The solid-mesh boundary was observed through SEM (Fig. 3a), which clearly showed the detachment of boundary mesh structure from the solid body. In Fig. 3b, the mesh fracture can be easily located on the center of the head part.

In order to characterize the fracture behavior of Ti-6Al-4V, fractographical analysis was performed, as shown in Fig. 4. Tiny gas pores, which functioned as the crack initiation sites, were observed in the ductile ruptured area in the *XY*-H axis specimen (Fig. 4a-1 and 4a-3). In the vicinity of the shear fractured area near the surface, pores and relatively large gas pores were observed, which decreased the tensile elongation (Fig. 4a-2 and 4a-4). The initial voids were formed in the center of the specimen owing to the triaxial stress condition, and later these voids grew and coalesced to form a crack. Moreover, cracks originated from the cluster of unmelt powders, leading to unstable crack propagation (Fig. 4b-4). In addition, the specimen broke into irregular cup and cone shapes, and the location of the fracture was not

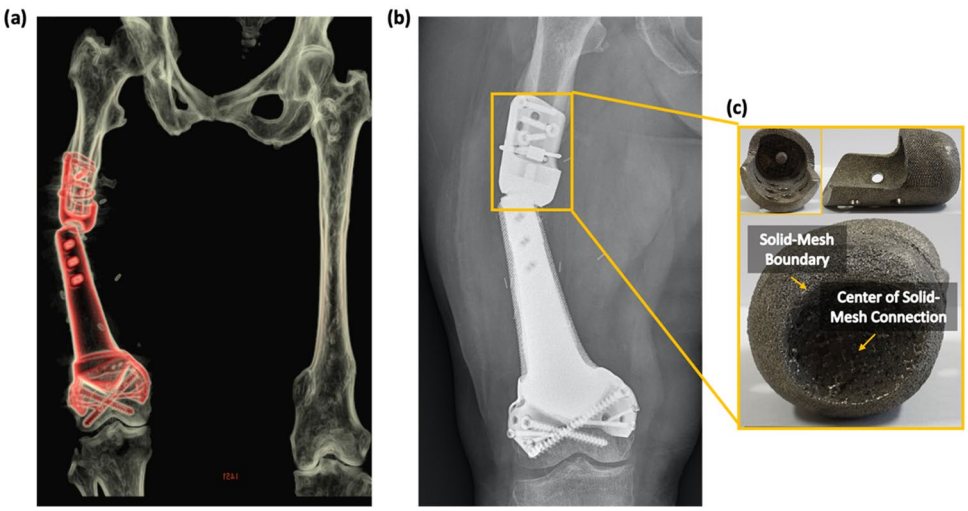

Fig. 2 Fracture of Ti-6Al-4V implant 6 months post-surgery. **a** Computed tomography reconstruction image, **b** plain radiography (X-ray), **c** fractured head part of implant (fractured solid-mesh boundary area, fractured center area of solid-mesh connection)

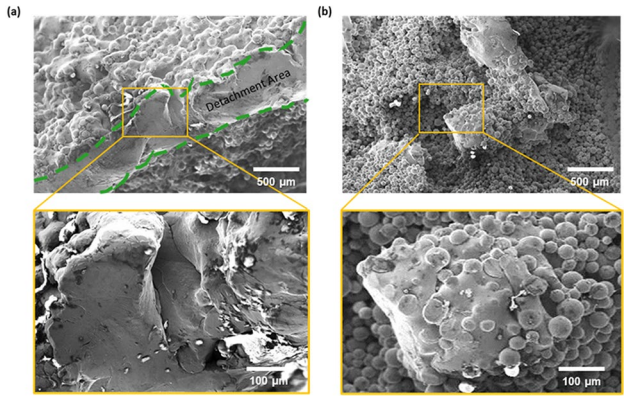

Fig. 3 Scanning electron microscopy (SEM) of the fractured implant; **a** boundary area, **b** center area

constant. In the *Z*-axis specimen, a shear lip surrounded the entire specimen, whereas the shear lip was discontinuous in the *XY*-H specimen. Therefore, crack bursting occurred toward the surface of the specimen in the *XY*-H specimen, which decreased the tensile elongation.

For the mechanical analysis (Fig. 5), both the plate- and round-type specimens were subjected to tensile testing. The center part of the plate tensile specimen was designed as a mesh structure to determine the strength of the mesh body. Round-type tensile specimens printed in the *XY*-H direction and *Z*-axis direction were designed to measure the strength of the Ti-6Al-4V alloy fabricated with the EBM 3D printer. The *XY*-H axis specimens were built along the *XY* plane. The side with the longest length was placed on the *XY* plane as the height along the *Z* direction. The *Z*-axis specimens were fabricated along the *Z* direction where the longest side was placed on the *Z*-axis. The stress–strain curves of the tensile specimens manufactured using the EBM 3D printer indicated that both types of mesh specimens were destroyed without reaching the plastic deformation stage. As indicated in Table 1, the yield strengths of the mesh-type specimens were only 33 and 54 MPa, while the yield strengths of the solid-type specimens ranged from 970 to 1000 MPa. The results indicated that although the strength of implants printed on the EBM 3D printer was sufficient, the model was poorly formed when the mesh structure was included. To verify the main reason of such poor elongation of the mesh-type specimen, microstructural analysis was conducted for both the solid- and mesh-type specimens for comparison. Figure 6 shows the microstructures of *XY*-H and *Z*-axis solid-type specimens. In the figure, typical Widmanstätten microstructures can be observed with lamellar and colony structures, and their texture was developed along the building direction. Thus, owing to their perpendicular orientation, the *XY*-H specimen and *Z*-axis specimen naturally exhibited a (111) and (110) texture, respectively. Figure 7 presents the microstructures of the mesh-type specimen, which exhibits an α'-martensite microstructure with narrow laths. As a solid structure, the α'-martensite is more brittle than a Widmanstätten α-lamellar structure, hence the mesh-type specimen could have poor elongation properties compared to the solid-type specimen. Subsequently, a computer-aided

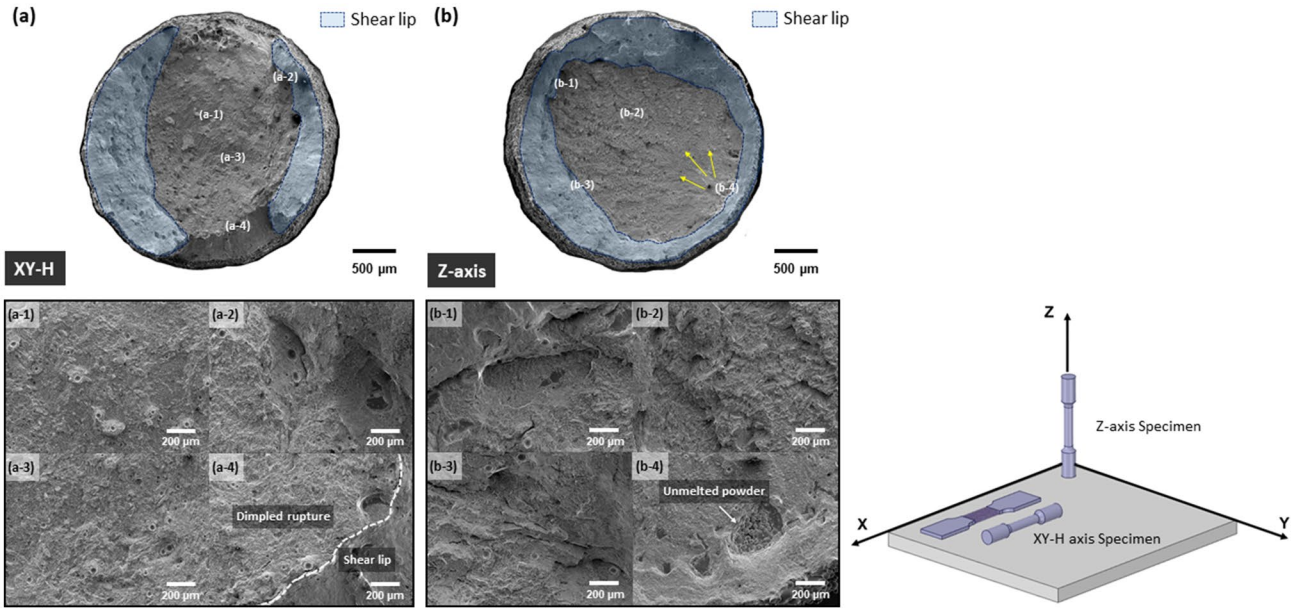

Fig. 4 Fractography of the tensile test specimens. **a** *XY*-H axis, **b** *Z*-axis

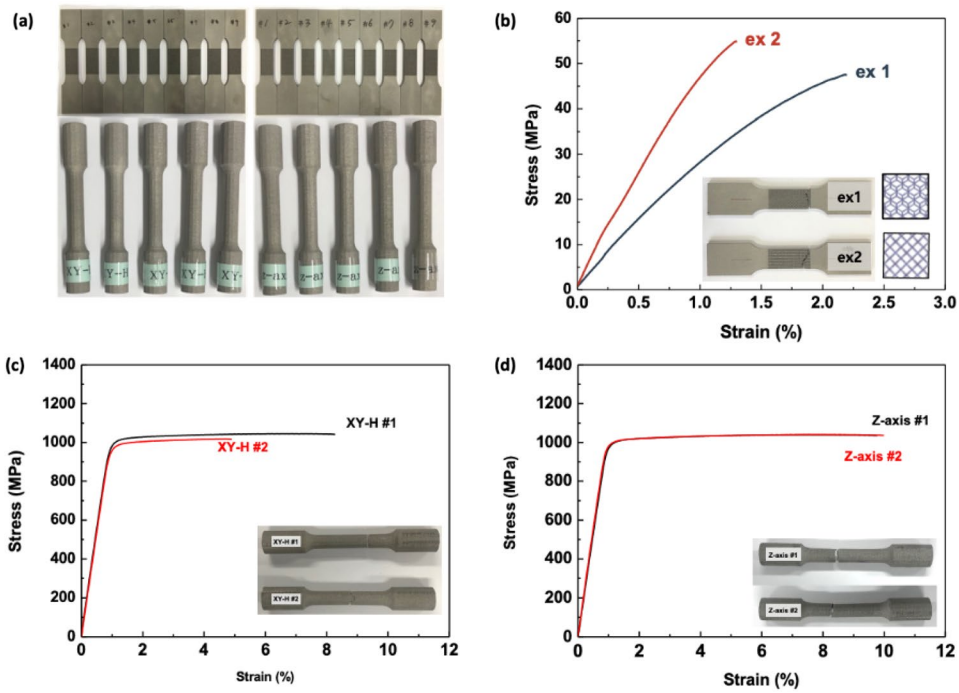

Fig. 5 Characterization of mechanical properties of the EBMed Ti-6Al-4V specimen. **a** ASTM-E8 standard (round-type and plate-type) specimens, **b** stress–strain curve of mesh-type specimen, **c** stress–strain curve of round-type specimen (built along the *XY* plane), **d** stress–strain curve of round-type specimen (built along the *Z*-axis)

Table 1 Tensile tests for the ASTM-E8 standard specimen

Specimen ID	Yield strength (MPa)	Tensile strength (MPa)	Elongation (%)
ex1 #1	33	47	0.7
ex2 #1	54	55	0.2
XY-H #1	1000	1044	7.3
XY-H #2	976	1018	3.9
Z-axis #1	992	1039	8.8
Z-axis #2	995	1040	9.1

engineering analysis was conducted for the characterization of mesh-solid hybrid specimen and the implant under practical application.

The solid-mesh hybrid structure was simulated under various conditions (Fig. 8). The relative length and cut surface area ratio between the solid and mesh structures were set as 1:2 for length and 20–100%, respectively, as shown in Fig. 8a. The Von Mises stress generally tended to concentrate on the boundary area of solid and mesh structure, as shown in Fig. 8b. As seen in Fig. 8c, the axial load angle varied from 0° to 90° for each of the 20%, 40%, and 60% mesh case. The maximum Von Mises stress at the boundary of mesh and solid for the 60% mesh case was relatively higher than the other cases for every force input angle. The maximum Von Mises stress tended to saturate as the input force angle approached 90°. When the relative mesh length was doubled, this saturation behavior also appeared for the 20% mesh area case. However, the saturation behavior tended to disappear for the 40% and 60% mesh cases, which indicates that there is a certain mesh ratio where the maximum Von Mises stress does not reach an excessive value under high-angle force input. For further simulation with practical force input, the direction and amount of force were derived from a personalized body model using the commercial software (AnyBody Modeling System, Denmark), as shown in Fig. 9c and 9d. The condition of fast gait was simulated through finite element analysis (FEA) to examine the harshest environment for verifying the stability of the implant. In particular, in the FEA simulation, the distal femur was fixed, and external force was applied to the proximal femur head. Based on the actual physiological loading of the human body, two conditions were assumed: fast gait and limping gait, and two cases were considered for both conditions. The direction and angle of force for the two conditions were based on the data obtained from the AnyBody modeling system.

Figures 9a and 9b show the input composition of the implants and the boundary condition for simulation. The Von Mises stress on three parts, namely the full body, mesh body, and solid hole, was simulated in the analysis as shown in Fig. 9a. In Table 2, the maximum Von Mises stress in the fast gait 1 and 2 conditions was 1013.9 and 2030.8 MPa, respectively, and its value in the limping gait 1 and 2 conditions was 883.41 and 802.21 MPa, respectively. The largest Von Mises stress corresponded to the fast gait 2 condition. Moreover, in this condition, the stress was 329.52 and 2000.4 MPa in the mesh body and solid hole part, respectively. The stress was concentrated on the

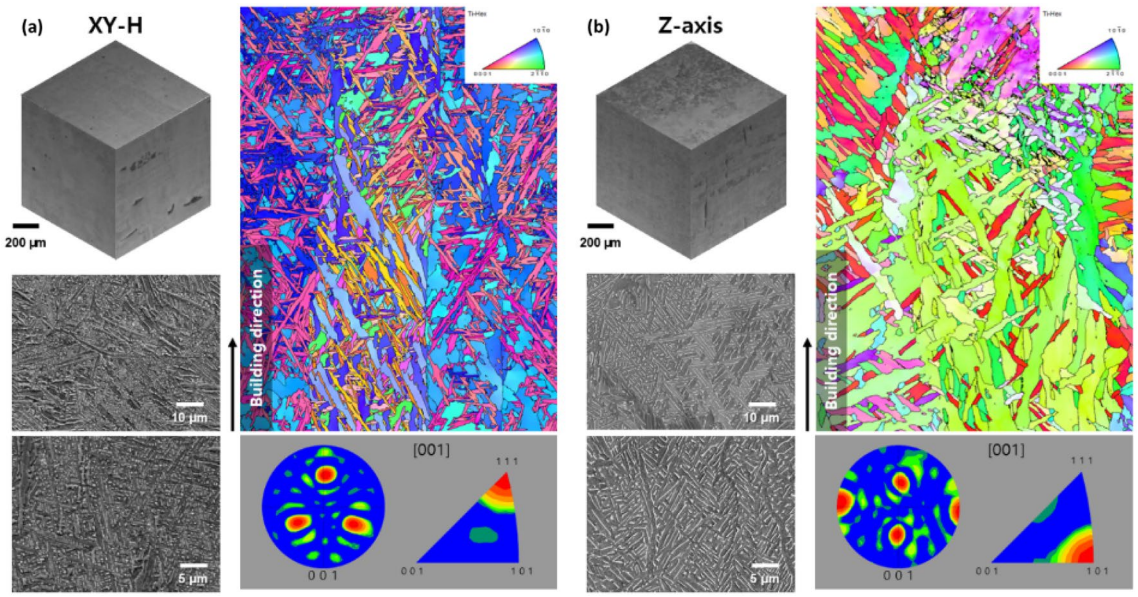

Fig. 6 Solid tensile electron backscatter diffraction (EBSD) characterization of specimen along the **a** *XY*-H axis, **b** *Z*-axis

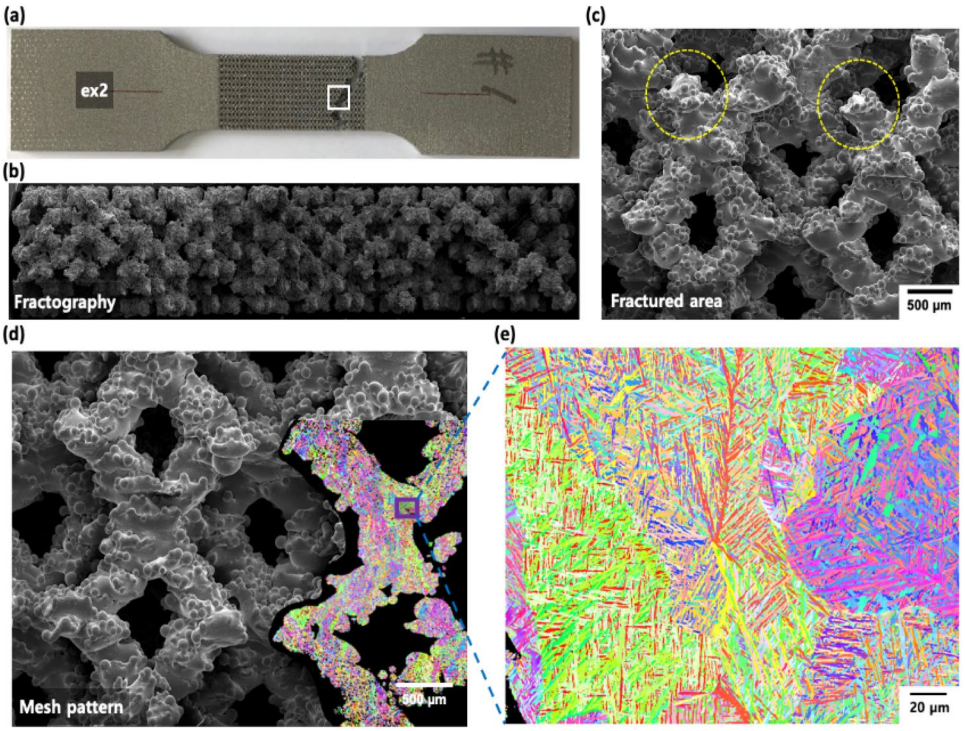

Fig. 7 Microstructural analysis of mesh structure of the tensile specimens. **a** Mesh-type tensile specimen, **b** fractography of mesh specimen, **c** extended view of fractured area, **d** EBSD overlapped mesh structure, **e** extended view of EBSD of mesh structure

upper part of the mesh body, which formed the connection between the head part and solid hole body. Overall, the computational analysis indicated that the fracture of the implant was partly due to the physiological loading of the human body, and the stress was concentrated in the head-body connection. While these in-depth simulations should be done prior to the surgery, the time limitation of urgent cancer replacement surgery consists a bottleneck to performing sufficient simulations. These limitations shall be addressed in our future work by obtaining a big data pre-simulation platform for most possible fractures of 3D-printed implants.

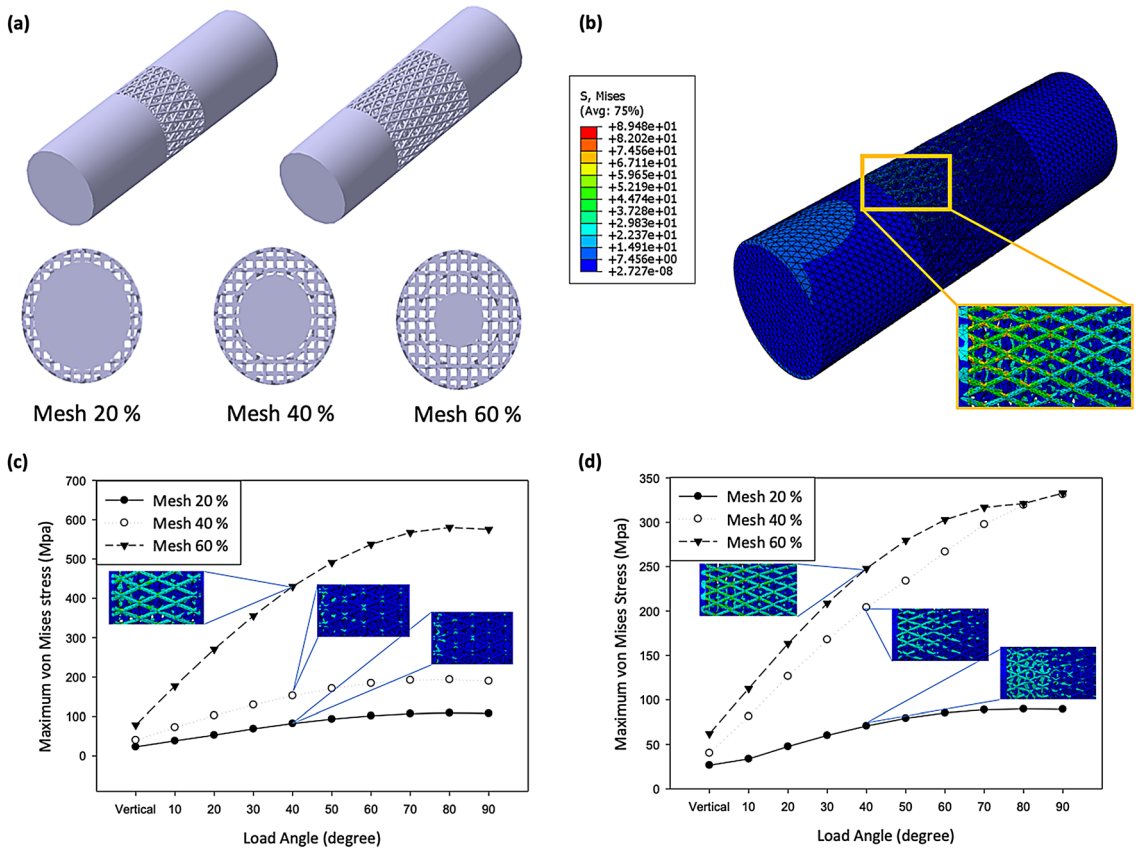

Fig. 8 FEA result for mesh structure content and load angle. **a** Six types of 3D specimens were used in the FEA: 20 mm and 40 mm in length, and with 20%, 40%, and 60% of mesh ratio. **b** One example of the FEA result. The stress was concentrated on the mesh structure of the central region. **c** Maximum Von Mises stress according to mesh structure contents and load angle of 500 N at 20 mm and **d** 40 mm length

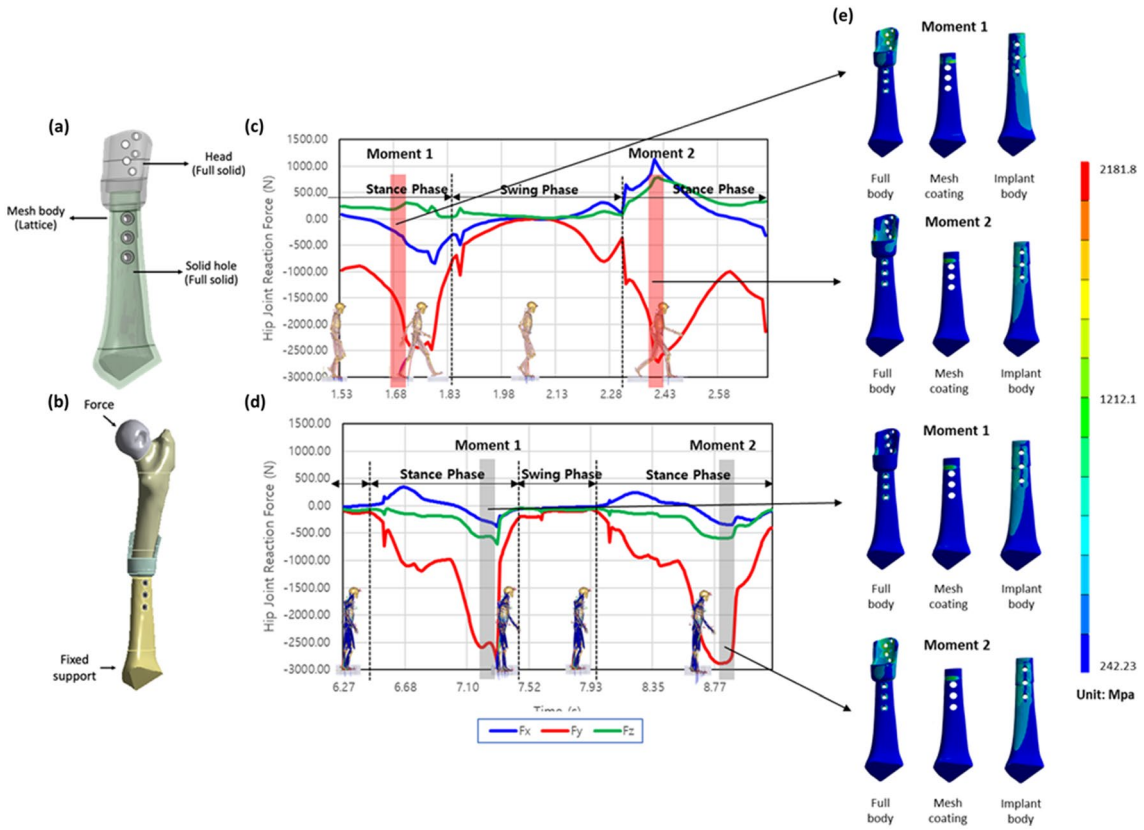

Fig. 9 Configuration for computational analysis. **a** Implant composition for input parameter in simulation. **b** Boundary condition in the FEA. **c–e** Joint reaction force analysis; **c** fast gait, **d** limping gait, **e** FEA result for the implant

Table 2 Analysis results of right hip joint reaction

Type of gait	Time (s)	Force (N)		
		F_x	F_y	F_z
Fast 1	1.72	−516.26	−2406.36	302.08
Fast 2	2.41	1007.22	−2716.50	791.81
Limping 1	7.80	−379.53	−2884.16	−699.10
Limping 2	8.85	−347.42	−2860.48	−590.91

Conclusions

The customized Ti-6Al-4V implant supported the 6-week recovery of a patient from bone cancer while preserving the original joint and made them able to walk normally for half a year. Due to a minor downward slip, the in situ implant suffered fracture. The comprehensive mechanical, microstructural, and computational analysis of the customized Ti-6Al-4V implant revealed that the in situ fracture might have occurred mainly for two reasons: microstructural aspect and implant design. Despite the possibility of crack initiation due to unmelt powder, the solid Ti-6Al-4V had sufficient mechanical strength with Widmanstätten α-lamellar structure to tolerate the body weight in the long-term. On the other hand, the mesh Ti-6Al-4V had poor elongation characteristics with brittle α'-martensite microstructure featured by narrow laths. Excessive stress concentration was also detected near the brittle mesh and solid connection area within the designed implant, which made the brittle mesh structure unable to withstand the physiological loading pattern of human walking. While these thorough simulations provide insight into the design of artificial bio-implants for bone cancer treatment, a pre-simulation big data platform is necessary for a quick assessment of designed implants prior to cancerous bone replacement surgery. Once bone cancer has been diagnosed, there is a strict time limitation for treatment, thus lengthy in-depth CAE analyses are not feasible. Future research encompassing the aforementioned pre-simulated big data platform should provide guidelines for mesh and solid structure designs that can withstand the physiological loading patterns of different types of patients to facilitate better surgical outcomes. Our groundwork of the detailed inspection of a 3D-printed implant and subsequent failure analysis provides guidance for the design of more durable patient-customized Ti-6Al-4V implants with the appropriate consideration of different mechanical/microstructural

properties of mesh and solid structure for enhanced practical application.

Acknowledgements This study was supported by the National Cancer Center Grant (No. NCC-2110270), the Ulsan National Institute of Science and Technology (No. 1.200110.01), and the National Research Foundation of Korea (NRF) Grant funded by the Korea government (MSIP) (No. 2018R1A5A6075959) and the Korea government (MSIT) (No. 2021M2D2A1A01050059). Special thanks to June Hyuk Kim (Orthopaedic Oncology Clinic, National Cancer Center) and Do Young Park (CMET Company) for supporting the projects.

Author contributions JWP and IDJ were involved in conceptualization; JWP, YCS, SP, ES, HS, and IDJ performed formal analysis; HGK and IDJ conducted supervision; JWP and HGK contributed to funding acquisition; JWP and HS conducted investigation; YCS, SP, ES, HS, and IDJ contributed to visualization. JWP, ES, HS and IDJ were involved in writing—original draft; JWP and IDJ were involved in writing review and editing.

Declarations

Conflict of interest The authors declare that there is no conflict of interest.

Ethical approval All procedures followed were in accordance with the ethical standards of the responsible committee on human experimentation (institutional and national) and with the Helsinki Declaration of 1975, as revised in 2008 (5).

Informed consent Informed consent was obtained from all patients for being included in the study.

References

1. Mitchell A, Lafont U, Hołyńska M et al (2018) Additive manufacturing—a review of 4D printing and future applications. Addit Manuf 24:606–626. https://doi.org/10.1016/j.addma.2018.10.038
2. Bhavar V, Kattire P, Patil V et al (2014) A review on powder bed fusion technology of metal additive manufacturing. In: 4th international conference and exhibition on additive manufacturing technologies-AM-2014, pp 1–2
3. Froes F, Dutta B (2014) The additive manufacturing (AM) of titanium alloys. Adv Mater Res 1019:19–25. https://doi.org/10.1016/B978-0-12-800054-0.00024-1
4. Liu A, Xue G, Sun M et al (2016) 3D printing surgical implants at the clinic: a experimental study on anterior cruciate ligament reconstruction. Sci Rep 6:21704. https://doi.org/10.1038/srep21704
5. Dawood A, Marti BM, Sauret-Jackson V (2015) 3D printing in dentistry. Br Dent J 219(11):521–529. https://doi.org/10.1038/sj.bdj.2015.914
6. Jung J, Lee J, Cho D (2016) Computer-aided multiple-head 3D printing system for printing of heterogeneous organ/tissue constructs. Sci Rep 6:21685. https://doi.org/10.1038/srep21685
7. Yang F, Chen C, Zhou Q et al (2017) Laser beam melting 3D printing of Ti6Al4V based porous structured dental implants: fabrication, biocompatibility analysis and photoelastic study. Sci Rep 7:45360. https://doi.org/10.1038/srep45360
8. Zhang B, Pei X, Zhou C et al (2018) The biomimetic design and 3D printing of customized mechanical properties porous Ti6Al4V scaffold for load-bearing bone reconstruction. Mater Des 152(15):30–39. https://doi.org/10.1016/j.matdes.2018.04.065
9. Zhao L, Pei X, Jiang L et al (2019) Bionic design and 3D Printing of porous titanium alloy scaffolds for bone tissue repair. Compos B Eng 162:154–161. https://doi.org/10.1016/j.compositesb.2018.10.094
10. Song P, Hu C, Pei X et al (2019) Dual modulation on crystallinity and macro/micro structures of 3D printed porous titanium implants to enhance the stability and osseointegration. J Mater Chem B 7(17):2865–2877. https://doi.org/10.1039/C9TB00093C
11. Pei X, Wu L, Zhou C et al (2021) 3D printed titanium scaffolds with homogeneous diamond-like structures mimicking that of the osteocyte microenvironment and its bone regeneration study. Biofabrication 13:015008. https://doi.org/10.1088/1758-5090/abc060
12. Lei H, Yi T, Fan H et al (2021) Customized additive manufacturing of porous Ti6Al4V scaffold with micro-topological structures to regulate cell behavior in bone tissue engineering. Mater Sci Eng C Mater Bio Appl 120:111789. https://doi.org/10.1016/j.msec.2020.111789
13. Chen Y, Bian L, Zhou H et al (2010) Usefulness of three-dimensional printing of superior mesenteric vessels in right hemicolon cancer surgery. Sci Rep 10(1):11660. https://doi.org/10.1038/s41598-020-68578-y
14. Guan B, Wang H, Xu R et al (2016) Establishing antibacterial multilayer films on the surface of direct metal laser sintered titanium primed with phase-transited lysozyme. Sci Rep 6:36408. https://doi.org/10.1038/srep36408
15. Yan L, Lim J, Lee J et al (2020) Finite element analysis of bone and implant stresses for customized 3D-printed orthopaedic implants in fracture fixation. Med Biol Eng Comput 58(5):921–931. https://doi.org/10.1007/s11517-019-02104-9
16. Ma L, Zhou Y, Zhu Y et al (2017) 3D printed personalized titanium plates improve clinical outcome in microwave ablation of bone tumors around the knee. Sci Rep 7(1):7626. https://doi.org/10.1038/s41598-017-07243-3
17. Harrysson OLA, Cormier DR (2006) Advanced manufacturing technology for medical applications: reverse engineering, software conversion and rapid prototyping. In: Gibson I (ed) Direct fabrication of custom orthopedic implants using electron beam melting technology. Springer, Berlin, pp 191–206
18. Parthasarathy J, Starly B, Raman S et al (2010) Mechanical evaluation of porous titanium (Ti6Al4V) structures with electron beam melting (EBM). J Mech Behav Biomed Mater 3(3):249–259. https://doi.org/10.1016/j.jmbbm.2009.10.006
19. Choy WJ, Mobbs RJ, Wilcox B et al (2017) Reconstruction of thoracic spine using a personalized 3D-printed vertebral body in adolescent with T9 primary bone tumor. World Neurosurg 105:1032.e13-1032.e17. https://doi.org/10.1016/j.wneu.2017.05.133
20. Park JW, Kang HG, Lim KM et al (2018) Three-dimensionally printed personalized implant design and reconstructive surgery for a bone tumor of the calcaneus: a case report. JBJS Case Connect 8(2):e25. https://doi.org/10.2106/JBJS.CC.17.00212
21. Kotz R (1993) Tumor endoprosthesis in malignant bone tumors. Der Orthop 22(3):160–166
22. Kim Y, Jang WY, Park JW et al (2020) Transepiphyseal resection for osteosarcoma in patients with open physes using MRI assessment. Bone Joint J 102(6):772–778. https://doi.org/10.1302/0301-620X.102B6.BJJ-2019-1141.R2
23. Eleutério SJ, Senerchia AA, Almeida MT et al (2015) Osteosarcoma in patients younger than 12 years old without metastases

have similar prognosis as adolescent and young adults. Pediatr Blood Cancer 62(7):1209–1213. https://doi.org/10.1002/pbc.25459
24. Park JW, Kang HG, Kim JH et al (2021) The application of 3D-printing technology in pelvic bone tumor surgery. J Orthop Sci 26(2):276–283. https://doi.org/10.1016/j.jos.2020.03.004
25. Park JW, Kang HG, Kim JH et al (2020) New 3-dimensional implant application as an alternative to allograft in limb salvage surgery: a technical note on 10 cases. Acta Orthop 4:489–496. https://doi.org/10.1080/17453674.2020.1755543
26. Angelini A, Trovarelli G, Berizzi A et al (2019) Three-dimension-printed custom-made prosthetic reconstructions: from revision surgery to oncologic reconstructions. Int Orthop 43(1):123–132. https://doi.org/10.1007/s00264-018-4232-0
27. Liang H, Ji T, Zhang Y et al (2017) Reconstruction with 3D-printed pelvic endoprostheses after resection of a pelvic tumour. Bone Joint J 99(2):267–275. https://doi.org/10.1302/0301-620X.99B2.BJJ-2016-0654.R1
28. Tsuboyama T, Windhager R, Dock W et al (1993) Knee function after operation for malignancy of the distal femur: quadriceps muscle mass and knee extension strength in 21 patients with hinged endoprostheses. Acta Orthop Scand 64(6):673–677. https://doi.org/10.3109/17453679308994596
29. Holm I, Nordsletten L, Steen H et al (1994) Muscle function after mid-shaft femoral shortening. A prospective study with a two-year follow-up. J Bone Joint Surg Br 76(1):143–146. https://doi.org/10.1302/0301-620X.76B1.8300660